Annals of Nuclear Medicine Vol. 17, No. 2, 99–106, 2003

Dependency of energy and spatial distributions of photons on edge of object in brain SPECT

Hossain M. DELOAR, Hiroshi WATABE, Nobuyuki KUDOMI, Kyeong Min KIM, Toshiyuki AOI and Hidehiro IIDA

Department of Investigative Radiology, National Cardiovascular Center Research Institute

Objectives: Accurate μ maps are important for quantitative image reconstruction in SPECT. The Compton scatter energy window (CSW) technique has been proposed to define the outline of objects. In this technique, a lower energy window image is acquired in addition to the main photo-peak energy window. The image of the lower energy window is used to estimate the edge of the scanned object to produce a constant attenuation map. The aim of this study was to investigate the dependency of CSW on the spatial and energy distribution of radioisotope to predict the edges of objects. ***Methods:*** Two particular cases of brain study were considered, namely uniform distribution and non-uniform distribution using Monte Carlo simulation and experiments with uniform cylindrical phantom and hotspot phantom. The phantoms were filled with water and a radioactive solution of ^{99m}Tc. For each phantom, 20%, 30%, 40% and 50% thresholds of the mean profile were applied to estimate E_{wt}, the energy window for minimum difference between the estimated and true edge of objects. ***Results:*** The E_{wt}'s were 100–120 keV with a 40% threshold and 92–114 keV with a 30% threshold for uniform and hotspot phantoms, respectively. ***Conclusions:*** Edge of the objects with CSW technique varies with energy window and thresholds. Careful setting of the energy window is required to use the CSW technique.

Key words: attenuation map, SPECT quantification, Compton scatter energy window, edge of object, threshold

INTRODUCTION

ATTENUATION μ MAP is essential to quantify cerebral functions using Single Photon Emission Computed Tomography (SPECT).[1–6] It is possible to obtain a μ map by anatomical image-based measurements from magnetic resonance imaging (MRI) and computed tomography (CT),[7–10] or by transmission scans.[2,11,12] Anatomical image-based measurements require additional measurements with limited clinical applicability and that can also produce systematic errors due to movement of the subject between scans. Simultaneous transmission scan may produce an ideal μ map with minimal additional scan. But sophisticated hardware is required. Additional radiation exposure to patients is another disadvantage of this method.

The Compton scatter window (CSW) technique has been proposed to estimate the edges of objects.[13,14] The CSW technique does not require anatomical images (from CT and MRI) or transmission scans to produce the attenuation map. In this technique, a lower energy window image is acquired simultaneously with an image of the main photo-peak energy window, and the lower energy image is employed to estimate the edge of the scanned object to produce a constant attenuation map. This technique does not require an additional scan and is feasible for most clinical SPECT systems.

In general, Compton scattered photons are broadly distributed, and the outline of objects can be depicted using edge detection techniques on the CSW image.[13,14] However, the spatial and energy distributions of Compton

Received September 20, 2002, revision accepted December 19, 2002.

For reprint contact: Hiroshi Watabe, Ph.D., Department of Investigative Radiology, National Cardiovascular Center Research Institute, 5–7–1 Fujishirodai, Suita, Osaka 565–8565, JAPAN.

E-mail: watabe@ri.ncvc.go.jp

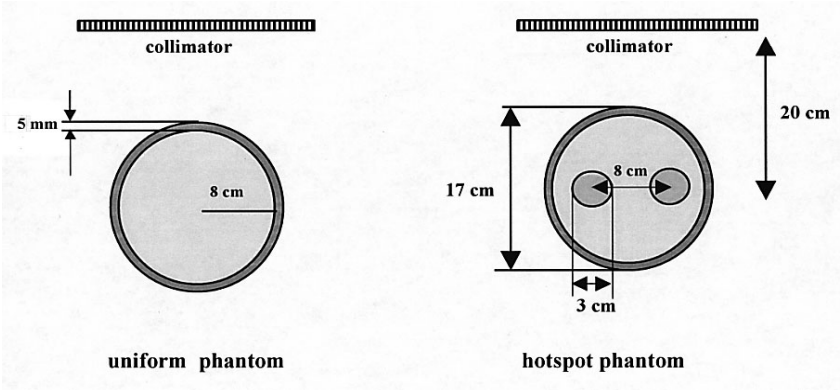

Fig. 1 Cross-sectional views for the geometry of uniform and non-uniform (hotspot) phantom with collimator in simulation and experimental. The inner diameter of the uniform phantom was 16 cm and height was 20 cm with a wall thickness of 5 mm. The phantom was filled with water and ^{99m}Tc solution. In hotspot phantom two hotspots filled with ^{99m}Tc solution were placed in the water filled uniform phantom in such a way that the center of each was 8 cm apart from each other, dimension of hotspot was 5 cm long and 3 cm diameter.

scattered photons depend on the energy and spatial distributions of radioisotopes in the object, which must be considered to obtain the best results by using the CSW technique. In the study of Ben Younes et al.[13] an energy window from 92 to 125 keV was used for the uniform distribution of ^{99m}Tc radioisotope. Pan et al.[14] suggested to use 99–120 keV of Compton energy window among five energy windows (120–130, 109–130, 99–130, 99–120 and 99–109 keV) to estimate the edge of the chest region with CSW technique.

Our study aimed to investigate the dependency of the energy window in CSW technique to obtain edges of objects for two types of radioisotope distribution, namely uniform and non-uniform (hotspot), which mimic perfusion study[3,4,15] and dopamine study[8,16,17] for brain SPECT, respectively. Simulations and experiments were carried out using the uniform and non-uniform distributions. The MCNP4C code[18] was used for Monte-Carlo simulations and the simulated data were validated against experimental results.

METHODS

The experimental and simulated cross-sectional views of the geometry of the uniform and hotspot phantoms are shown in Figure 1.

A. Simulation

The MCNP (version C) is an efficient Monte Carlo code for photon transport calculations.[18] With the generalized input card of MCNP the user can specify a variety of source and detector conditions by creating a proper geometry. The source, spectrum of the radiation source, configuration and composition of the medium for radiation transportation, and collimator geometry can be defined in the input card.[18] Acquisition of gamma camera system for uniform and hotspot phantoms with a ^{99m}Tc source were simulated by MCNP code. In the gamma camera detection system, an energy dependent Gaussian-shaped energy resolution (11% at 140 keV) were assumed for the detector. Corrections of energy dependent detection efficiency was introduced for the NaI(Tl) crystal of thickness 9.5 mm. The data of energy resolution and detection efficiency were obtained from the previous study.[19] For simplicity, a cylindrical lead collimator of 25 mm diameter and 40 mm length was modeled instead of a hexagonal collimator. Thickness of the collimator wall was 1 mm,[19] and the NaI(Tl) crystal was placed behind the collimator in such a way that only photons incident on the detector with an acceptance angle of $\pm 2.1°$ with respect to the normal passing through the center of the detector elements could be detected.[19] The collimator positions and phantom geometry are shown in Figure 1.

The uniform phantom was cylindrical with a 16 cm inner diameter, and the wall thickness and height of the phantom were 5 mm and 20 cm, respectively. For the hotspot phantom, two cylinders, 3 cm diameter and 5 cm long, filled with ^{99m}Tc solution were placed inside the water-filled uniform phantom so that the centers of the hotspots were on the phantom's central line 8 cm apart. Two environments were considered for hotspot phantoms. In one case, the water-filled phantom was free of background radioactivity and in the other case 3%, 5%, 8% and 10% activity of the hotspots was mixed with water, and filled the cylindrical phantom. Radioactivity concentration for the uniform and hotspot phantom was 0.06 μCi-sec/m*l* and 3.8 μCi-sec/m*l*, respectively. The total (primary and scatter) photon flux of various energies from the phantom were detected and stored in the energy bin. Further simulations of hotspot phantom were carried out to see the dependency of energy window on count statistics by generating the radioactivity of 0.38 μCi-sec/

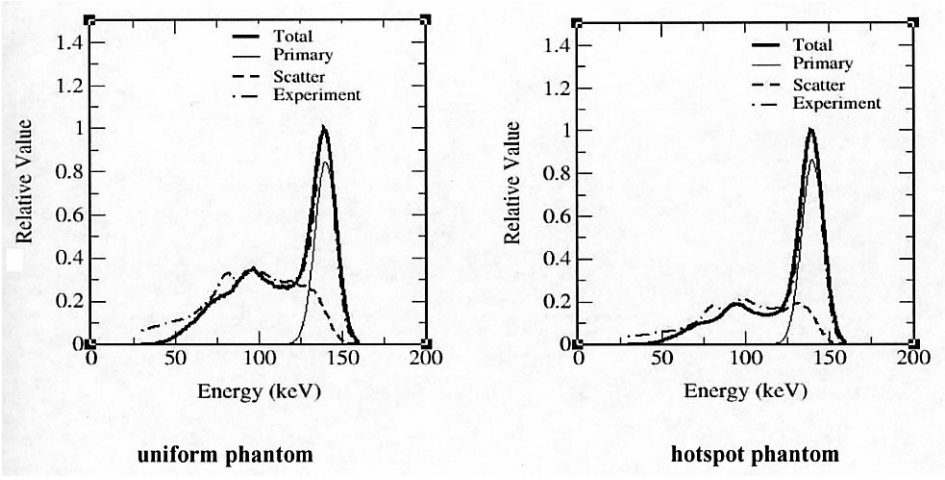

Fig. 2 Simulated and experimental energy spectra for uniform and hotspot phantom. Thick solid line, thin solid line and dashed line corresponds simulated total, primary and scatter components, respectively, dot-dashed line is the experimental total spectra.

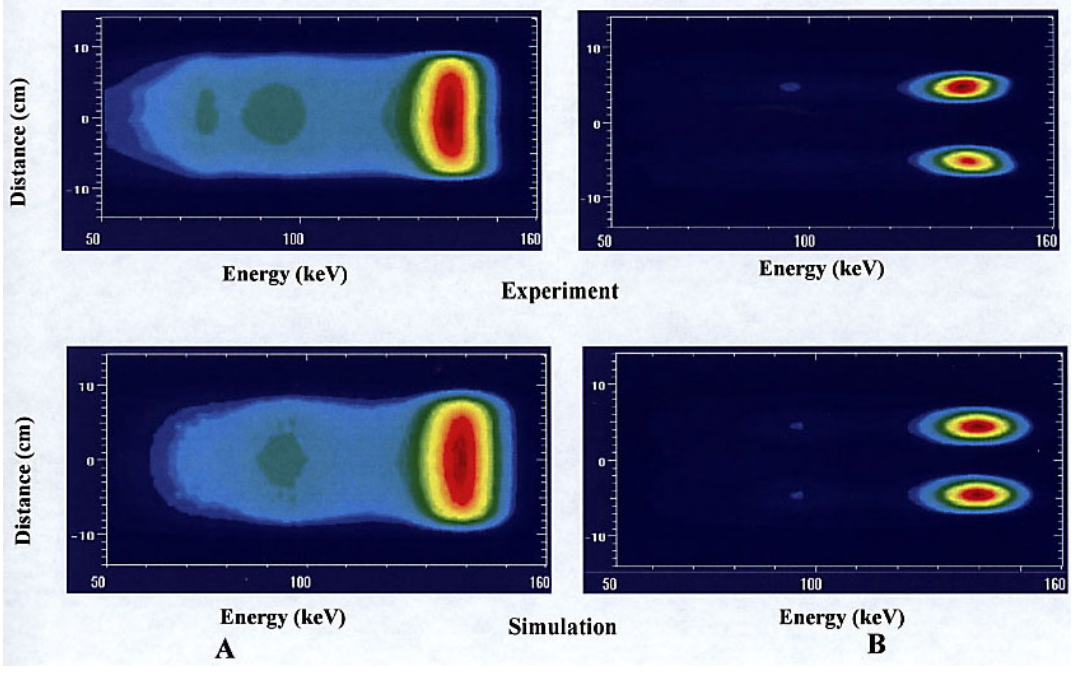

Fig. 3 Distribution of photons with energy for uniform (A) and non-uniform (hotspot) (B) phantom. Tops are experimental and bottoms are simulated photon distributions for uniform and hotspot phantom.

m*l* and 38 μCi-sec/m*l*, in addition to 3.8 μCi-sec/m*l*. The data were arranged in the form of two-dimensional matrices, $M(l,e)$, where l is the location of the detector and e is the photon energy (50 keV < e < 160 keV) from the ^{99m}Tc source. The $M(l,e)$ represented the spatial and energy distributions of the photons. Twenty sets of $M(l,e)$ were generated from the data set of each simulation and with their corresponding standard deviation (from MCNP calculation), and these generations of data sets were used to evaluate the standard deviation of the investigated energy window.

B. Phantom experiment

Experiments with water-filled uniform and hotspot phantoms were performed with ^{99m}Tc radioactive sources to validate the simulations. Radioactivity concentration in the uniform phantom was 0.47 μCi/m*l* and for hotspot phantom the concentration was 15 μCi/m*l*. Experimental acquisitions were made with a single-head SPECT system (Toshiba, GCA-7100A, Japan). A parallel hole collimator, NDCL-701A, LEHR (Low Energy High Resolution) was used in the experiment. The distance between the center of the phantom and surface of the collimator was approximately 20 cm. With the Toshiba SPECT system it

Table 1 Simulated and experimental E_{wt} (the energy window for minimum A i.e. minimum difference between the estimated and true edge of objects) in various thresholds for uniform phantom and their $A(E_u,E_w)$ values from Eq. 3

Threshold (%)	Simulation Activity 0.06 μCi/ml		Experiment Activity 0.47 μCi/ml	
	E_{wt} (keV)	*$A(E_u,E_w)$ (mm)	E_{wt} (keV)	*$A(E_u,E_w)$ (mm)
20	124–125	2.86 ± 0.28	124–125	0.09
30	112–124	1.60 ± 0.04	111–125	0.10
40	100–121	0.17 ± 0.02	101–119	0.10
50	107–111	1.38 ± 0.12	106–111	1.60

* $A(E_u,E_w)$ is the lowest difference between estimated and true edge

Table 2 Simulated and experimental E_{wt} (the energy window for minimum A i.e. minimum difference between the estimated and true edge of objects) in various thresholds for hotspots phantom and their $A(E_u,E_w)$ values from Eq. 3

Threshold (%)	Simulation						Experiment Activity 15 μCi/ml	
	Activity 0.38 μCi/ml		Activity 3.8 μCi/ml		Activity 38 μCi/ml			
	E_{wt} (keV)	*$A(E_u,E_w)$ (mm)	E_{wt} (keV)	*$A(E_u,E_w)$ (mm)	E_{wt} (keV)	*$A(E_u,E_w)$ (mm)	E_{wt} (keV)	*$A(E_u,E_w)$ (mm)
20	124–125	2.96 ± 1.32	124–125	0.20 ± 0.02	124–125	0.19 ± 0.01	113–125	0.06
30	89–109	1.72 ± 1.12	90–112	0.19 ± 0.01	91–112	0.04 ± 0.01	92–114	0.07
40	103–105	1.84 ± 0.76	109–110	0.21 ± 0.02	111–112	0.49 ± 0.20	107–108	0.65
50	109–110	1.92 ± 0.72	109–112	2.84 ± 0.04	111–112	3.04 ± 0.15	105–106	2.50

* $A(E_u,E_w)$ is the lowest differences between estimated and true edge

is possible to acquire images simultaneously for all energies of the emitted photons. Planar images for both the uniform and hotspot phantoms were acquired for energies from 50–160 keV with an interval of 1.6 keV. The acquisition time was 20 minutes. The matrix size of the image was 128 × 128, and pixel size was 4.3 mm.

C. Data analysis

The edge of the object was determined from both the simulated and experimental data. One-dimensional profiles, $P(l,E_u,E_w)$ with a given energy window from $E_u - E_w$ to E_u were computed from $M(l,e)$ by varying two parameters of the upper energy thresholds, E_u (81–126 keV) and energy window width E_w (1–46 keV), as follows:

$$P(l,E_u,E_w) = \sum_{e=E_u-E_w}^{E_u} M(l,e) \qquad \text{Eq. 1}$$

Since 126 keV is the lower limit of the energy window of 20% photo-peak of 140 keV, to investigate the E_wt's in CSW technique energy above 126 keV was not considered. A threshold technique was used to estimate the edges of the object. Threshold technique has been investigated to detect the edges of objects considering a threshold of maximum pixel counts within a volume.[20] In this study we applied the threshold technique in a different form. The one-dimensional ratio profile $R_p(l, E_u, E_w)$ was calculated as

$$R_P(l,E_u,E_w) = P(l,E_u,E_w) \,/\, \overline{P(l,E_u,E_w)} \qquad \text{Eq. 2}$$

where $\overline{P(l,E_u,E_w)}$ is the mean profile along location, l. To obtain estimated edges (left or right), 20%, 30%, 40% and 50% thresholds on $R_p(l,E_u,E_w)$ were applied in such a way that the locations (left and right sides) of the threshold value along l were searched for. The agreements, $A(E_u,E_w)$, at a given energy window between the estimated and true edges were evaluated using the following equation:

$$A(E_u,E_w) = \frac{\sqrt{(e_l - t_l)^2 + (e_r - t_r)^2}}{2} \qquad \text{Eq. 3}$$

where e_l, e_r and t_l, t_r are the estimated and true edges of left and right sides of the object, respectively. The lowest value of A was determined within the energy range from $E_u - E_w$ to E_u. The *energy window with the least difference between the estimated and true edge of objects* (E_{wt}) gave the lowest value of A.

RESULTS

The simulated energy spectra $\left(\sum_{l=-12.8}^{l=12.8} M(l,e)\right)$ for total, scattered and primary contributions for both uniform and hotspots phantoms are shown in Figure 2 and compared with experimental spectrum. Using a ^{99m}Tc isotope, experiments with uniform and hotspot phantoms were performed to acquire planer images from 50–160 keV with an interval of 1.6 keV. Those images gave information on the spatial and energy distribution of photons. The planer images were used to obtain the energy spectrum (Fig. 2) as well as the profile counts for measurement of edges in

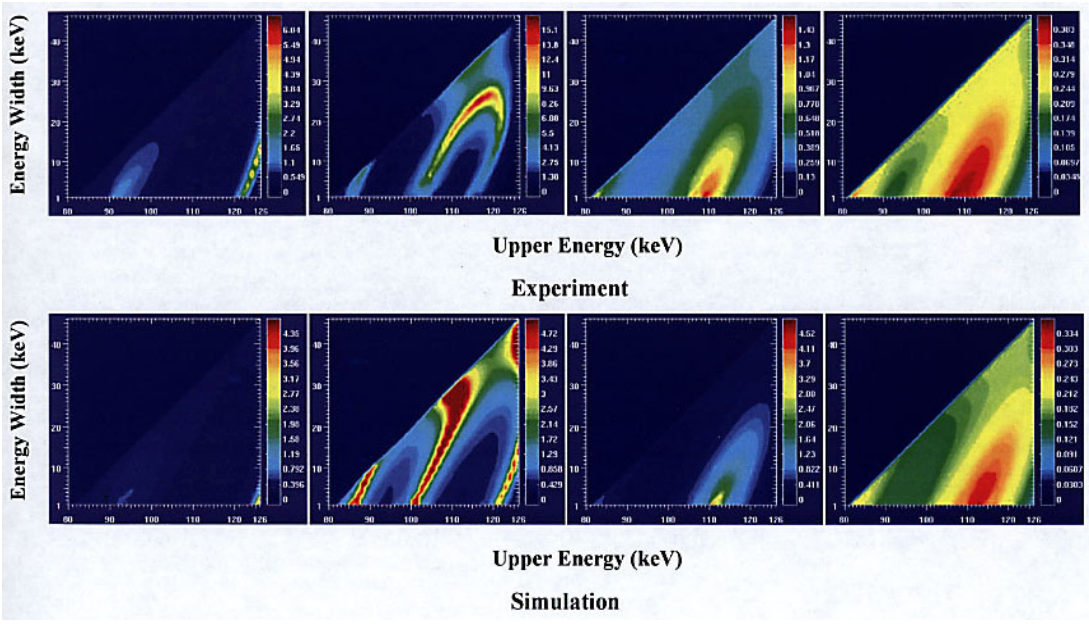

Fig. 4 Two dimensional plots of $1/A$ (Eq. 3) for the hotspots phantom for various thresholds (from left 20%, 30%, 40% and 50%) using radioactivity of 3.8 μCi/ml.

various energy windows. The simulated total spectra were comparable with the experimental spectrum except at the lower energy region. In simulations, the contributions of KX-rays from a lead collimator at the lower energy region were not considered. Two-dimensional plots of energy and spatial distributions of total photons for both the uniform and hotspot phantoms are shown in Figure 3. The distribution of photons in the simulations and experiments were very similar, except near an energy of 80 keV with KX-rays. Variations in the distribution of photons can be found with photon energy for both of the phantoms.

One-dimensional profiles, as described above (in Methods, section C), were calculated to find the edges of the phantoms. By searching for the lowest value of A from 20 set of $M(l,e)$ the E_{wt}'s for various thresholds were estimated. The mean values of A with their standard deviation were computed and the corresponding E_{wt}'s for uniform and hotspot phantoms are shown in Tables 1 and 2. An example of two-dimensional plots of $1/A$ (with 3.8 μCi/ml) for hotspot phantom using various thresholds is shown in Figure 4. The absolute values of $1/A$ in Figure 4 appear at the right side with a color scale. In the figures it was clearly seen that the A varied with the energy window and thresholds. The lowest value of A can provide the best edges of the phantoms and depends on radioisotope distribution in the object, as shown in Figure 4.

The simulated lowest value of A in Table 1 for the uniform phantom for various thresholds (20%, 30%, 40% and 50%) was different from the experimental values. But the E_{wt}'s appearing at all thresholds were very similar to the experimental results, those values being 124–125 keV for the 20% thresholds, 111–125 keV for 30% thresholds, 100–121 keV for 40% thresholds and 106–111 keV for 50% thresholds. For the uniform distribution of photons the E_{wt} obtained from the 40% thresholds might be useful due to its wider energy width as well as lower standard deviation and consistency of results with experiment and simulation.

For hotspot phantoms, the simulated E_{wt}'s for all thresholds in Table 2 and Figure 4 are comparable to the experimental values except for some minor differences. The simulated and experimental E_{wt}'s for various radioactivities are also shown in Table 2. At the same threshold, the lowest value of A for simulations with different radioactivities were different. With increasing radiactivities the differences between the estimated edge and actual edges estimated from Eq. 3 decreases i.e. the lowest value of A decreased. In Table 2, all the simulated E_{wt}'s with a 20% threshold were similar among three different radioactivity concentrations but different from the experimental E_{wt}. For the 30% threshold the E_{wt}'s of different radioactivity concentrations in simulations were comparable with the experimental results, although the absolute values of A were different in all cases. For 30% threshold, in simulation the appeared energy window was 90–112 keV but in the experiment that value was 92–114 keV. Although at 30% threshold a relatively high value of $1/A$ appeared at various energy settings as shown in Figure 4, only the energy windows having the lowest value of A are shown in Table 2. The E_{wt} for 40% and 50% thresholds were very narrow in all cases. The 30% threshold might be useful to detect the edge of the hotspot objects because simulated E_{wt}'s with 30% thresholds using various radioactivity concentrations are mutually consistent and consistent with experiment results also. Furthermore, the

standard deviation of A for 30% threshold was lower than that of the other thresholds.

To simulate a real environment, 3%, 5%, 8% and 10% activities with respect to the activity of hotspot phantom (3.8 μCi-sec/ml) were considered as background. For all backgrounds, the lowest absolute value of A was different but the E_{wt}'s were the same as the E_{wt} without background (Fig. 4).

DISCUSSION

Dependency of the estimated edge of objects using CSW technique was investigated in the Compton energy region for the radioactivity distributions of ^{99m}Tc nuclide. Usually in the CSW technique a 20% photo-peak window (126–154 keV for 140 keV from ^{99m}Tc nuclide) and another window in the Compton energy region are used. Thus this study was designed to determine the dependency of edge of objects on all possible energy windows below the 20% photo-peak energy window (80–126 keV).

In our study we demonstrated the energy dependency of the edge of objects for CSW technique with Monte Carlo simulations and experiments. Since Toshiba's SPECT system can provide the pixel-wise energy spectra, the Monte Carlo simulation results were compared with the experimental results. Monte Carlo simulation is a powerful tool to simulate any SPECT system. Monte Carlo simulations to investigate the dependency of the edge of objects with CSW technique will be helpful for those SPECT systems which can not provide the pixel-wise energy spectra.

Hotspot phantom was simulated for 0.38 mCi/ml, 3.8 mCi/ml and 38 mCi/ml, to see the effect of radioactivities on E_{wt}. As shown in Table 2, the absolute value of A depends on the amount of radioactivities but the E_{wt} windows are almost independent of radioactivities. Higher radioactivities can provide the data with less statistical noise, whereas low radioactivity produces noisy data as a result the absolute values of A estimated from the higher radioactivities providing minimum A with respect to the data of low radioactivity. In the previous study,[14] the proposed best energy window was 99–120 keV in order to get the best contour of the lung as well as body to produce attenuation map. Our study on uniform distribution shows a similar best energy window, which was 100–120 keV, but for the hotspot distribution the E_{wt} was 92–112 keV.

To evaluate the value of A, the energy range of 80–126 keV was considered (Fig. 3). Energy below 80 keV was not considered to avoid background photons from various sources, such as scatter photons from the bed, walls, etc. In the simulations the PM tubes and other necessary circuits were not modeled, and their effects may also have created some differences between the experimental and simulated results. Contributions of KX-rays from lead collimators, backscatter photons from the PM tube and scatter photons from the bed were not considered in the simulated data. In Figure 4 the experimental 30% A map was slightly different from the simulated A map. This is due to the KX-rays from the collimator in the experiments. The simulated results were free from the KX-rays. SPECT performance usually depends on several parameters, including geometric efficiency, intrinsic efficiency, and geometry of the collimator hole, especially the shape, length and diameter of the collimator. A mismatch of any of the parameters in the simulation may affect the simulated result and eventually produce some discrepancies between the experimental and simulated spectra, as well as in the spatial distribution of radioisotopes, as shown in Figures 2 and 3. Nonetheless, good agreements between the simulated and experimental results were observed.

We used A as an evaluation function of the mismatch between the true edges and estimated edges of objects for CSW technique. In order to examine the relationship between A values and error in emission images, attenuation maps with different A values (2, 4.3, 8,6, 12.9 and 17.2 mm) were generated for the uniform phantom with a diameter of 17 cm. Emission images were reconstructed with all of the attenuation maps using an ordered subset expectation maximization (OSEM) reconstruction algorithm and 1%, 2.5%, 7.5%, 10.5% and 13.6% errors were observed in the reconstructed images for A values of 2, 4.3, 8,6, 12.9 and 17.2 mm, respectively. The attenuation map from E_{wt} will be able to provide emission images with less than 2% error.

The threshold technique has been used to detect the edges of uniform objects.[20,21] In the reported studies a threshold (%) of the maximum count in the profile was considered to fix a threshold. However, if the profile counts are statistically very noisy, a marked variation may occur in the maximum count. Therefore, in this study, we employed mean profile counts (Eq. 2) as the index of thresholds, which are less sensitive to noise. Usually the threshold technique is an arbitrary technique and several threshold techniques can be found in the literature.[13,14,20,21] Therefore, the value of threshold may be different in different threshold techniques to investigate the E_{wt} in CSW techniques. We have investigated the various thresholds to find the best contour of the edge of objects, and the absolute values of A with their corresponding standard deviation for various thresholds are shown in Tables 1 and 2. Among the thresholds, 40% threshold was found to be good with a wider energy window and low value of standard deviation for uniform distribution, and consequently for hotspot distribution the 30% threshold gave wider energy window with less standard deviation. Note that although we have shown the energy window setting with the lowest A for various thresholds in Tables 1 and 2, this paper does not intend to propose the energy setting for clinical use of CSW technique. We emphasize rather the strong dependency of spatial and energy distribution of radioisotope on the energy setting with CSW technique. Thus, special care

must be taken to determine the energy window especially for the case of clinical study of non-uniform distribution.

Using ^{99m}Tc, variation in the distribution of radioisotopes with energy for edge detection was demonstrated in this study for two specific cases of phantoms. This distribution may vary with other type of radioisotopes and source geometry. Further investigations are needed to determine the distribution of isotopes and actual settings E_{wt} in clinical studies with different radioisotopes.

CONCLUSIONS

This study demonstrated that variations of spatial and energy distributions of emitted photons affect the outline of an object. The edge of the object varies with the width of the energy window in Compton scatter energy window (CSW) technique. Use of CSW technique for detecting the best edge of an object requires the setting of a proper energy window. This study demonstrated that for uniform distribution an energy window in between 100–120 keV with a 40% threshold is good enough to obtain the edge of the object and for hotspot E_{wt} is 92–115 keV with a 30% threshold. Depending on the threshold techniques, the value of threshold and E_{wt} may be changed. Therefore, for each technique a prior investigation needs to confirm the E_{wt} for clinical use. Especially in cases in which radioisotope distribution is similar to the hotspot phantom (i.e. oncology and dopamine studies), careful setting of the energy window is required.

ACKNOWLEDGMENT

This research was supported by the research Grant for Cardiovascular Disease (12-12C) from the Ministry of Health Labour and Welfare.

REFERENCES

1. Iida H, Narita Y, Kado H, Kashikura A, Sugawara S, Shoji Y, et al. Effects of scatter and attenuation correction on quantitative assessment of regional cerebral blood flow with SPECT. *J Nucl Med* 1998; 39: 181–189.
2. Licho R, Glick SJ, Xia W, Pan TS, Penney BC, King MA. Attenuation compensation in ^{99m}Tc SPECT brain imaging: a comparison of the use of attenuation maps derived from transmission versus emission data in normal scans. *J Nucl Med* 1999; 40: 456–463.
3. Kado H, Iida H, Kimura H, Ogawa T, Narita Y, Hatazawa J, et al. Brain perfusion SPECT study with ^{99m}Tc-bicisate: clinical pitfalls and improved diagnostic accuracy with a combination of and scatter-attenuation correction. *Ann Nucl Med* 2001; 15: 123–129.
4. Kauppinen T, Koskinen MO, Alenius S, Vanninen E, Kuikka JT. Improvement of brain perfusion SPET using iterative reconstruction with scatter and non-uniform attenuation correction. *Eur J Nucl Med* 2000; 27: 1380–1386.
5. Galt JR, Cullom SJ, Garcia EV. SPECT quantification: a simplified method of attenuation and scatter correction for cardiac imaging. *J Nucl Med* 1992; 33: 2232–2237.
6. Hashimoto J, Sasaki T, Ogawa K, Kubo A, Motomura N, Ichihara T, et al. Effects of scatter and attenuation correction on quantitative analysis of beta-CIT brain SPET. *Nucl Med Commun* 1999; 20: 159–165.
7. Fleming JS. A technique for using CT images in attenuation correction and quantification in SPECT. *Nucl Med Commun* 1989; 10: 83–97.
8. Van Laere K, Koole M, D'Asseler Y, Versijpt J, Audenaert K, Dumont F, et al. Automated stereotactic standardization of brain SPECT receptor data using single-photon transmission images. *J Nucl Med* 2001; 42: 361–375.
9. Davis MH, Khotanzad A, Flamig DP, Harms SE. A physics-based coordinate transformation for 3-D image matching. *IEEE Trans Med Imaging* 1997; 16: 317–328.
10. Dey D, Slomka PJ, Hahn LJ, Kloiber R. Automatic three-dimensional multimodality registration using radionuclide transmission CT attenuation maps: a phantom study. *J Nucl Med* 1999; 40: 448–455.
11. Almquist H, Norrgren K, Palmer J, Jonson B, Wollmer P. Performance of simultaneous emission-transmission systems for attenuation-corrected SPECT: a method for validation applied to two camera systems. *Nucl Med Commun* 2001; 22: 759–766.
12. Bailey DL. Transmission scanning in emission tomography. *Eur J Nucl Med* 1998; 25: 774–787.
13. Ben Younes R, Mas J, Bidet R. A fully automated contour detection algorithm the preliminary step for scatter and attenuation compensation in SPECT. *Eur J Nucl Med* 1988; 14: 586–589.
14. Pan TS, King A, De Vries DJ, Ljungberg M. Segmentation of the body and lungs from Compton scatter and photo peak window data in SPECT: A Monte Carlo investigation. *IEEE Trans Med Imag* 1996; 15: 13–24.
15. Van Laere K, Versijpt J, Audenaert K, Koole M, Goethals I, Achten E, et al. ^{99m}Tc-ECD brain perfusion SPET: variability, asymmetry and effects of age and gender in healthy adults. *Eur J Nucl Med* 2001; 28: 873–887.
16. Kuikka JT, Tammela L, Bergstrom KA, Karhunen L, Uusitupa M, Tiihonen J. Effects of aging on serotonin transporters in healthy females. *Eur J Nucl Med* 2001; 28: 911–913.
17. Donnemiller E, Heilmann J, Wenning GK, Berger W, Decristoforo C, Moncayo R, et al. Brain perfusion scintigraphy with ^{99m}Tc-HMPAO or ^{99m}Tc-ECD and ^{123}I-beta-CIT single-photon emission tomography in dementia of the Alzheimer-type and diffuse Lewy body disease. *Eur J Nucl Med* 1997; 24: 320–325.
18. Briesmeister JF, ed. MCNPTM-A general Monte Carlo code for neutron and photon transport, Version 4C LA-13709-M, Los Alamos National Laboratory, 2000.
19. Narita Y. Transmission dependent convolution subtraction methods for correction of scattered photons in quantitative measurement by single photon CT and 3D positron CT Ph. D. thesis 1998, Dept. of Nucl. Eng. Tohoku University, Japan.
20. Pretorius PH, Aswegen VA, Herbst CH, Lotter MG. The effect of different correction techniques on absolute volume determination with SPECT using a threshold edge detection method. *Med Phys* 1991; 18: 390–393.

21. van Elmbt LR, Keyeux A, Demeure R. Validation of automated brain contour determination in normal and abnormal cerebral single-photon emission tomography. *Eur J Nucl Med* 1995; 22: 537–542.